Journal of Materials Chemistry A

ARTICLE

# From rational design of a new bimetallic MOF family with tunable linkers to an application case for OER catalyst

Received 00th January 20xx,
Accepted 00th January 20xx

DOI: 10.1039/x0xx00000x

www.rsc.org/

Xuan Zhang[a], Jiangshui Luo[a]*, Kai Wan[a], Dieter Plessers[b], Bert Sels[b], Jianxun Song[c], Liugang Chen[a,d], Ting Zhang[e], Pengyi Tang[e,f], Joan Ramon Morante[f], Jordi Arbiol[e,g]*, , Jan Fransaer[a]*

Innovative bimetallic MOFs offer more possibilities to further tailor the properties of MOFs, which have been attracted great attention for the wide applications. However, it is still a great challenge to rationally design bimetallic MOFs due to the lack of tunable and reasonable hybrid structure architecture. Herein, a new series of bimetallic metal-organic frameworks (MOFs) with tunable pillar linkers were prepared by a one-step synthesis method. These bimetallic MOFs retain the same crystal structure when the mole fraction (based on metal) of the two metals changes from 0 to 1 and both metal ions occupy uniform random nodal positions. The incorporation of a second metal cation has a large influence on the intrinsic properties (*e.g.* thermal stabilities and band gap) of the MOFs. Furthermore, these bimetallic MOFs were used as a self-sacrificial template to prepare bimetal oxide catalysts for oxygen evolution reaction (OER). After pyrolysis, a porous and hierarchical honeycomb-like structure with a carbon network covered (bi)metal oxides is formed. Among all the bimetallic MOF-derived catalysts, CoNi1@C showed the best performance for OER with the lowest Tafel slopes (55.6 mV $dec^{-1}$) and overpotential (335 mV on glassy carbon electrode and 276 mV on Ni foam) at a current density of 10 mA $cm^{-2}$, which is higher than state-of-the-art Co-Ni mixed oxide catalysts derived from MOFs for OER. Our results indicate that the incorporation of a second metal ion is a promising strategy to tailor the properties of MOFs. More importantly, this new bimetallic MOF family with tunable linkers is expected to serve as a flexible assembly platform to offer broad possibilities for the practical applications of MOFs.

## 1. Introduction

Metal-organic frameworks (MOFs), constructed by coordination bonds between metal ions (or clusters) and various organic linkers, show tunable pore sizes and components, highly ordered porous crystalline structures, and high surface areas. These characteristics make MOFs promising candidates for a wide range of applications, such as gas separation, gas storage, sensing, catalysis, energy storage and conversion, and versatile precursors for the preparation of nanomaterials.[1-4]

In order to further optimize the structure and properties, the incorporation of a second metal into the framework (*i.e.* bimetallic MOFs) is being explored recently.[5] The presence of a second metal in the framework changes the intrinsic properties of the MOFs significantly. For example, by incorporation of different metal ions into the structure of MOF-74, the resulting bimetallic MOF-74 showed very different gas adsorption and catalytic activity compared with the monometallic MOF-74.[6-9] In addition, the electronic properties of MOFs can be tailored by the metal node engineering, as shown in the recent work of Dolgopolova et al.[10] The stability, luminescence and magnetic properties of these bimetallic frameworks have also been investigated.[11-19] On the other hand, bimetallic MOFs show promise as self-sacrificial templates for preparing hybrid nanomaterials, which play an essential role in sensors, catalyst, energy storage and conversion applications. Huang and coworkers prepared porous $ZnO/ZnFe_2O_4/C$ octahedra with hollow interiors by using $Fe^{III}$ modified MOF-5 as the self-sacrificial template. The resulting material show good lithium-storage performance.[20] Recently, Ni–Co-mixed-oxide nanocages (prepared by using Prussian-blue-analog)[21] and carbon-coated $Co_xNi_{1-x}@Co_yNi_{1-y}O$ (prepared by MOF-74)[22] were successfully synthesized by using bimetallic MOFs as the self-sacrificial template. The resulting Co-Ni catalysts were used for oxygen evolution reaction (OER), which is currently a major bottleneck for electrochemical water splitting.[23] To generate a current density of 10 mA $cm^{-2}$,

[a] Department of Materials Engineering, KU Leuven, Leuven 3001, Belgium. E-mail: jan.fransaer@mtm.kuleuven.be; jiangshui.luo@gmail.com.
[b] Centre for Surface Chemistry and Catalysis, KU Leuven, Leuven 3001, Belgium.
[c] Henan Province Industrial Technology Research Institute of Resources and Materials, Zhengzhou University, 450001 Zhengzhou, China;
[d] Henan Key Laboratory of High Temperature Functional Ceramics, Zhengzhou University, Kexue Avenue 100, Zhengzhou, 450001, China
[e] Catalan Institute of Nanoscience and Nanotechnology (ICN2), CSIC and BIST, Campus UAB, Bellaterra, 08193 Barcelona, Catalonia, Spain. E-mail: arbiol@icrea.cat
[f] Catalonia Institute for Energy Research (IREC), Jardins de les Dones de Negre 1, Sant Adrià del Besòs, 08930 Barcelona, Catalonia, Spain
[g] ICREA, Pg. Lluís Companys 23, 08010 Barcelona, Catalonia, Spain
Electronic Supplementary Information (ESI) available: See DOI: 10.1039/x0xx00000x

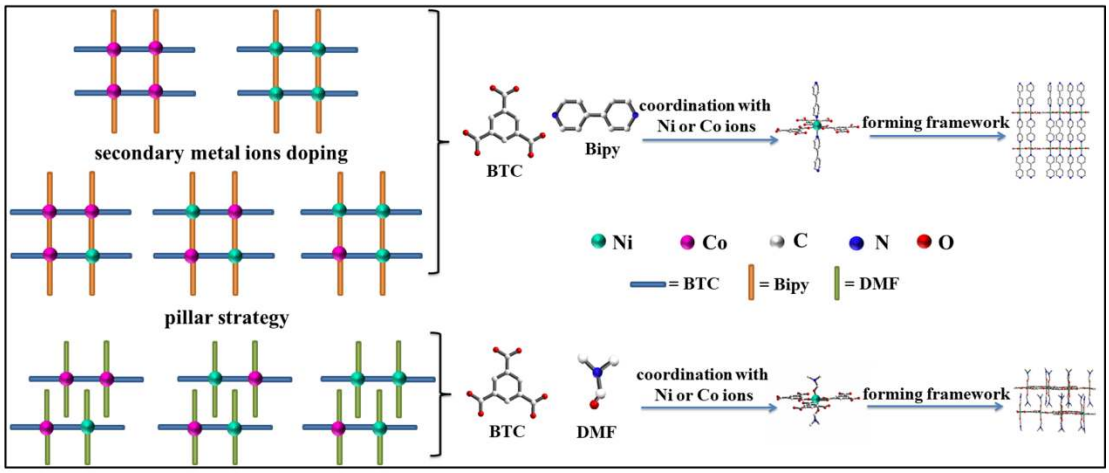


**Figure 1.** Schematic illustration of the synthesis of different bimetallic MOFs, perspective views of the crystal structure showing the coordinative environments around the MOF metal centers (all H atoms are omitted for clarity) and view of the supramolecular framework from the *b* axis

the overpotential for the Ni–Co-mixed-oxide nanocages and carbon-coated $Co_xNi_{1-x}@Co_yNi_{1-y}O$ were 380 mV and 520 mV, respectively. Meanwhile, other types of hybrid nanomaterials were also successfully prepared using bimetallic MOFs, such as core-shell structures and bimetallic nanoparticles.[24-30]

On the other hand, there are two general methods to prepare bimetallic MOFs: the one-step method and the post-treatment method. Although the post-treatment method can prepare bimetallic MOFs, it is difficult to rationally design the molar ratios of the two metals or to obtain a uniform random distribution of the two metal ions. Because of the small pore size and the large steric hindrance within MOFs, the exchange of metal ions needs to overcome large kinetic barriers and diffusion problems, leading to partial exchange in some cases. Moreover, when a second metal is introduced into a pristine MOF, the overall morphology of the MOF can change or even collapse.[31, 32] Until now, the one-step synthesis method is still the most effective way to achieve bimetallic MOFs. Unfortunately, bimetallic MOFs often have fragile frameworks as well as unpredictable topologies and functions after the introduction of new metal nodes. Some MOFs can remain their original structure when pristine MOFs are partially replaced by a second metal ion. For example, Botas et al. report that in the MOF-5 framework structure, only a limited amount of Zn can be substituted by $Co^{2+}$ (no more than 25% of the total metal mole content).[33] A similar situation happens with HKUST-1 and ZIF-8/ZIF-67.[34-38] Recently, some successful cases of bimetallic MOFs were reported by using Prussian-blue (PB) or Prussian-blue-analog (PBA) as prototypical MOFs, such as Co-Ni, Co-Fe, Co-Zn, Co-Mn, Fe-Mn and Fe-Ni.[39-46] However, the poor possibility for controlling pore size and linkers in PB and PBA are their key disadvantages. Compared to other MOFs, the most promising candidate is MOF-74. It can be easily designed for different Zn–Co mole fraction based on metal (from 0 to 1) by the one-step synthesis method.[6] Similarly, CoMg-MOF-74 and NiMg-MOF-74 have been synthesized successfully as well.[47] Interestingly, the pore size of MOF-74 can be precisely controlled from 1.4 to 9.8 nm by changing the number of phenylene rings in dioxidoterephthalate.[48] However, the further modifications are limited by the type of linkers, which hinder the potential applications of the MOF-74 family. Therefore, in order to investigate a broad range of possibilities for advanced applications of bimetallic MOFs, it would be advantageous to find an appropriate prototypical MOF that can serve as a flexible assembly platform.

Herein, we choose benzene-1,3,5-tricarboxylate (BTC) linker to form well-defined, two-dimensional (2D) plane layers with metal ions. By tailoring the pillars between the 2D layers, a series of bimetallic MOFs were successfully synthesized by the one-step synthesis method with different types of linkers. The chemical component and structure of bimetallic MOFs can be easily tailored by the pillar-linkers. These bimetallic MOFs keep their structure when the mole fraction mole fraction (calculation based on metal only) of the two metals changes from 0 to 1. Additionally, the properties of the resulting MOFs (such as thermal stabilities and band gap) change greatly with incorporating secondary metal nodes into the frameworks. Subsequently, different CoNi-BTC-bipy bimetallic MOFs were used as self-sacrificial templates to synthesize catalyst for OER. Pyrolysis led to the formation of carbon-metal oxides (or dual metal oxides) hybrid materials. Among all the bimetallic MOF-derived catalysts, CoNi1@C showed the lowest overpotential for OER (335 mV on a rotating disk electrode and 276 mV on Ni foam) at a current density of 10 mA $cm^{-2}$, which is higher than state-of-the-art Co-Ni mixed oxides catalysts derived from MOFs for OER.

## 2. Results and discussion

Benzene-1,3,5-tricarboxylate (BTC) linker based bimetallic MOFs have been successfully prepared by the one-step synthesis method. The coordination environment of the metal center for these two kinds of bimetallic MOFs are the same (**Figure 1**), where the nickel(II) or cobalt(II) center is bound by

 

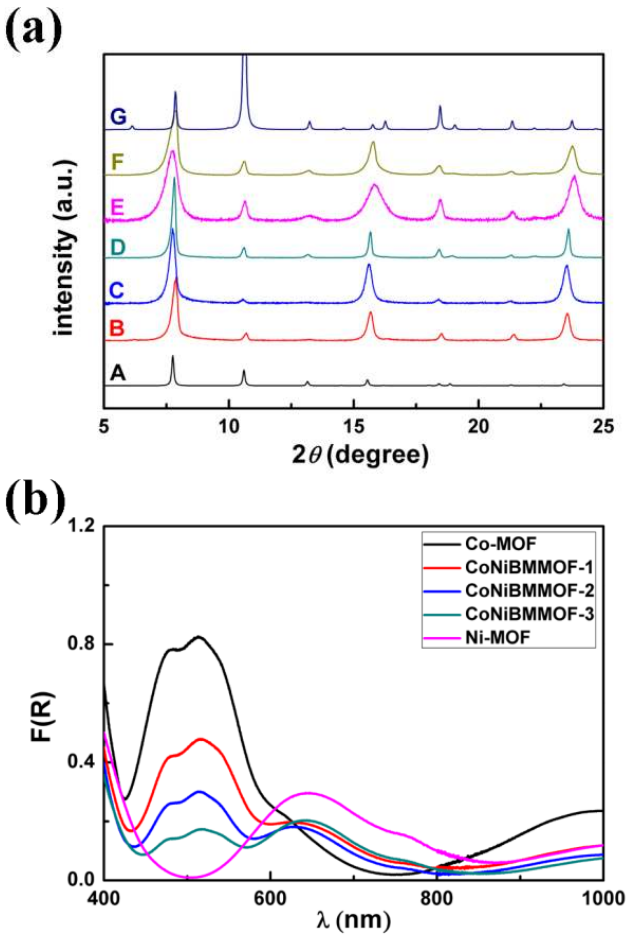


**Figure 3.** (*a*) Calculated XRD patterns of Co-MOF (A) and Ni-MOF (G), experimental XRD patterns of Co-MOF (B), CoNiBMMOF-1 (C), CoNiBMMOF-2 (D), CoNiBMMOF-3 (E) and Ni-MOF (F); (*b*) Diffuse reflectance UV-Vis spectroscopy of the different MOFs.

three BTC units with one bidentate carboxylic group and two monodentate carboxylic groups, which form a well-defined two-dimensional (2D) layer with honeycomb pores. The free carbonyls in the monodentate carboxylic groups are further bonded to a proton via hydrogen bond interactions, forming an overall neutral framework along the *ab*-plane. The polar positions of nickel(II) or cobalt(II) center are occupied by 4,4'-bipyridine along the *c* axis to form a 3D framework. In order to prove that this new family of bimetallic MOFs can be further tailored by ''pillaring'' strategy, a similar series of bimetallic MOFs based on DMF pillars were successfully prepared by the same method. The details of the basic characterizations (such as XRD, SEM and EDS) are shown in the **Figures S1-S2**. In this work, the bimetallic MOFs based on 4,4'-bipyridine are chosen as model MOFs for further study.

The crystalline structures of these synthesized MOFs are characterized by powder XRD (Figure 2a). The powder XRD patterns of all samples show identical characteristic diffraction peaks at 2θ ≈ 7.8°, 10.6°, 15.6° and 18.5°, which match well with the simulated patterns found in literature.[49] With the incorporation of a second metal in the frameworks, the crystal structure can be maintained even when the mole ratio of the two metals changes from 0 : 1 to 1 : 0. The metal contents (Co and Ni) in the prepared MOFs were determined by means of ICP-OES analysis (Figure S15). With increasing concentration of Ni in the starting solution, the content of Ni in MOF structure increases but the increase is not linear. This is caused by the different coordinating ability of $Co^{2+}$ and $Ni^{2+}$ towards the ligand.[49] The presence of a second metal in the MOFs was confirmed by diffuse reflectance UV-Vis spectroscopy (Figure 2). In all cases, the UV-Vis spectra are consistent with an octahedral coordination sphere for $Co^{2+}$ and $Ni^{2+}$. Indeed, the absorption bands at 450–550 nm and 650–670 nm, detected in the spectra of these MOFs, agree very well with the d-d transitions of $Co^{2+}$ and $Ni^{2+}$ in an octahedral coordination sphere, respectively.[9] The intensity changes of these absorption bands correspond to changes of the Co/Ni ratio in the prepared bimetallic MOFs, matching the changing content of Co and Ni precursors in the synthesis solution. These results indicate the bimetallic nature of these MOF materials. The band gaps of these MOFs were estimated by a plot of $\sqrt{F(R)h\nu}$ vs. energy[37, 38, 50, 51] from UV-Vis data for all samples (Figure S3). From the tangent lines in these plots, the band gaps of Co-MOF, CoNiBMMOF-1, CoNiBMMOF-2, CoNiBMMOF-3 and Ni-MOF were found to be 1.61 eV, 1.72 eV, 1.79 eV, 1.82 eV and 2.4 eV, respectively. Interestingly, the synthesized bimetallic MOFs also display evident color changes, depending on the ratio of the two metals (Figure S4). This tunable property of band gaps of bimetallic MOFs may also be promising for applications in photocatalysis.

In order to prove the uniform distribution of both metals inside the bimetallic MOFs, the relative metal element contributions of different bimetallic MOFs were analyzed by electron probe microanalysis (EPMA) coupled with wavelength dispersive spectroscopy (WDS). All the samples showed similar hexagon morphology (**Figure 3**). Moreover, the results of Co-Ni elemental relative composition mapping suggest a fairly homogenous distribution of Co and Ni throughout the hexagonal MOF sheets. The hexagon sheets show higher Co concentration than Ni, similar concentration for both Co and Ni and lower Co concentration than Ni for CoNiBMMOF-1, CoNiBMMOF-2 (c) and CoNiBMMOF-3, respectively (**Figure 3b-3d**). These results are in good agreement with the ICP-OES analysis, demonstrating that these bimetallic MOFs can form solid-solution type crystals over the whole concentration range.

Determination of thermal stabilities and decomposition temperatures of different MOFs were carried out via thermal gravimetric analysis (TGA) under nitrogen atmosphere. There are two main weight loss events during pyrolysis for all samples (**Figure S5**). The first one corresponds to the release of guest molecules (such as ethanol and DMF). The second event is likely attributed to the onset of the decomposition of the framework. The decomposition temperatures are 300 °C, 419 °C, 409 °C, 412 °C and 428 °C for Co-MOF, CoNiBMMOF-1, CoNiBMMOF-2, CoNiBMMOF-3 and Ni-MOF, respectively.

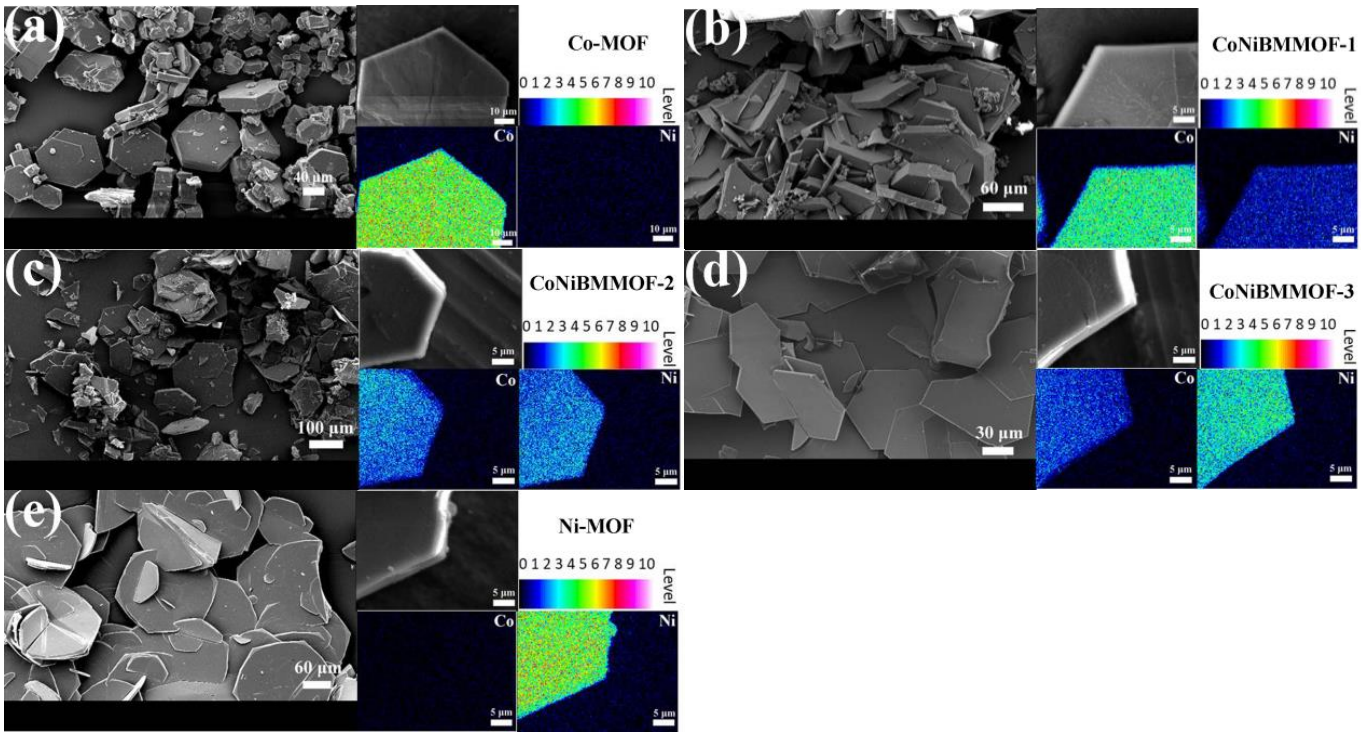


**Figure 3.** SEM and corresponding EMPA elemental mapping images for Co-MOF (*a*), CoNiBMMOF-1 (*b*), CoNiBMMOF-2 (*c*), CoNiBMMOF-3 (*d*) and Ni-MOF (*e*), respectively.

When Ni is added to the Co-MOF, the thermal stability of the MOFs increases significantly due to the higher coordination ability of $Ni^{2+}$ than $Co^{2+}$.[14, 49] Moreover, $Co^{2+}$ can be easily oxidized to $Co^{3+}$ at relatively low temperature.[33] After pyrolysis, all the samples retain their hexagon morphology (**Figure S6-S10**). At high magnification, a porous honeycomb-structure can be clearly observed, caused by the decomposition of the organic linkers. EDS confirmed that the different MOF derived catalysts contain C (originating from the organic linkers), O (from the formed metal oxide) and M (Co or Ni). The ratios of Co vs. Ni in the pyrolized MOFs are similar to the pristine MOFs. All samples were examined by XRD to confirm the crystalline phase (**Figure 4b**). The identified diffraction peaks of Ni@C and Co@C can be well indexed to NiO (JCPDS 65-2901) and $Co_3O_4$ (JCPDS 43-1003) with cubic structures, respectively. It is worth mentioning that for the bimetallic samples, the presence of spinel structure of $NiCo_2O_4$ (JCPDS 20-0781) could also be possible. For both the high Co or Ni ratio samples (*i.e.* CoNi1@C or CoNi3@C), the spinel phase dominates the crystalline phase. In addition, the coexistence of diffraction peaks of NiO and $Co_3O_4$ for CoNi2@C implies the formation of NiO and $Co_3O_4$ composites.

Furthermore, the chemical composition and valence state of Co and Ni are investigated by XPS measurements. The full scan survey XPS spectra of different catalysts in the region of 0−1000 eV (**Figure S11**) show evident C, O, Ni and Co peaks. The detailed chemical compositions based on full scan survey XPS spectra are summarised in **Table S1**. Additionally, the chemical states of Ni and Co in the catalysts were explored by high-resolution XPS spectra of Co 2p and Ni 2p (**Figure 5**). All cobalt-containing samples exhibit similar results. The binding

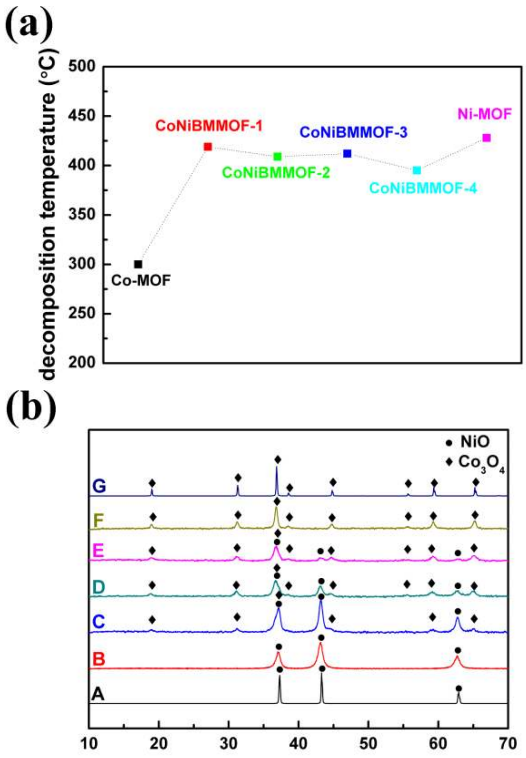


**Figure 4.** (*a*) Decomposition temperature of Co-MOF, CoNiBMMOF-1, CoNiBMMOF-2, CoNiBMMOF-3, and Ni-MOF obtained from TGA. (*b*) XRD pattern of NiO-JCPDS 65-2901 (A), Ni@C (B), CoNi3@C (C), CoNi2@C (D), CoNi1@C (E), Co@C (F) and $Co_3O_4$-JCPDS 43-1003 (G).

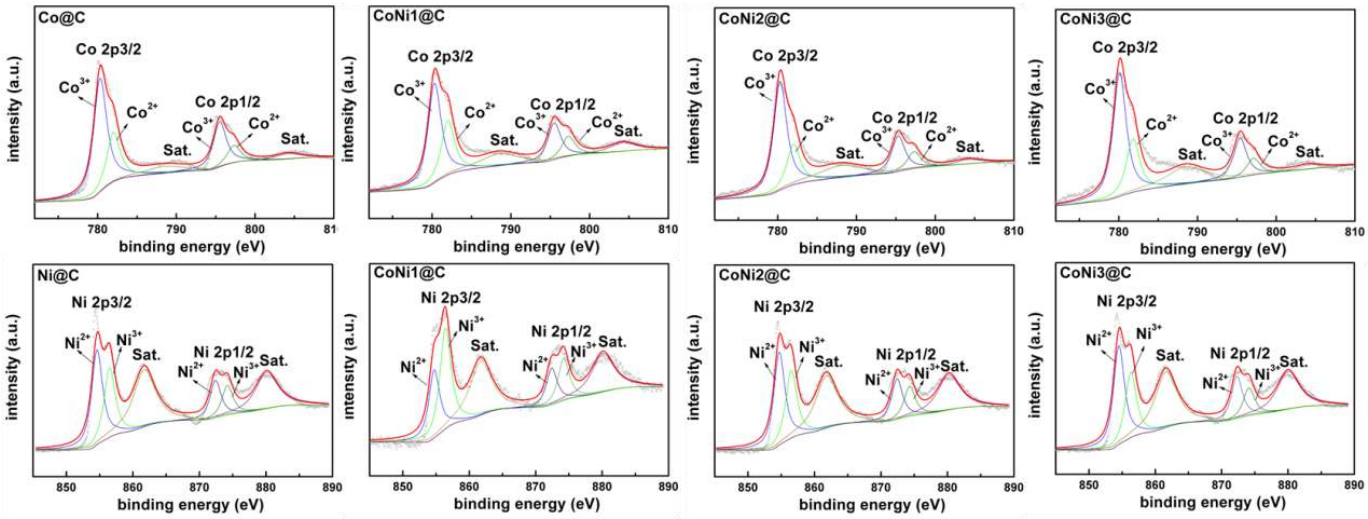


**Figure 5** High-resolution XPS spectra of Co 2p and Ni 2p for Co@C, CoNi1@C, CoNi2@C, CoNi3@C and Ni@C catalyst powders.

energies of Co 2p3/2 and Co 2p1/2 (**Figure 5**) show two spin-orbit doublets (corresponding to $Co^{2+}$ and $Co^{3+}$) at around 780.1 eV and 795.4 eV, respectively, with a spin energy difference of around 15.3 eV, indicating the presence of mainly $Co_3O_4$ phase. The weak shake-up satellite peaks for Co 2p spectra further reveal that the dominant phase is $Co_3O_4$.[52] In the spectra of Ni 2p, two pairs of spin-orbit doublets and two shake-up satellites can be clearly observed. More specifically, the peaks at 874.3 and 856.3 eV correspond to $Ni^{3+}$, while the peaks at 872.5 and 854.6 eV can be attributed to $Ni^{2+}$. For CoNi2@C, CoNi3@C and Ni@C, NiO is the dominant phase. Interestingly, CoNi1@C shows the opposite results with $Ni^{3+}$ as the dominant phase, which is probably because $Co_3O_4$ can induce the formation of $Ni^{3+}$ because in the presence of a high amount of cobalt, the $Ni^{3+}$ valence state can be stabilized.[53] It also implies the likely formation of a $Ni_3O_4$–$Co_3O_4$ solid solution at the calcination temperature of 500 °C.[53]

General HAADF STEM, TEM and HRTEM micrographs and EELS chemical composition maps of all the samples are shown in **Figure 6-7** and **Figure S12-S13**. The $Co_3O_4$ nanocrystals derived from the Co-MOFs (Co@C) are present as hexagonal-shaped nanostructures with a size around 20 nm–40 nm (**Figure 6a**). In addition, according to the HRTEM images, the $Co_3O_4$ nanocrystals derived from Co-MOFs show good crystallinity. A magnified detail of the orange squared region and its corresponding power spectrum reveal that the selected nanocrystal structure is in agreement with the cubic $Co_3O_4$ phase (space group *Fd3mz*) with $a = b = c = 0.806$ nm. Based on the crystalline domain shown in **Figure 6a**, the $Co_3O_4$ lattice fringe distances were measured to be 0.249 nm, 0.204 nm and 0.244 nm, respectively, with crystal plane angles of either 26.83º or 51.92º, which could be interpreted as the cubic $Co_3O_4$ phase that is visualized along its $[0\bar{1}1]$ zone axis. These results agree with XRD data. Similarly, the pure Ni-MOF derived catalyst (Ni@C) is in line with the NiO cubic phase (space group *Fm3m*) with $a = b = c = 0.420$ nm (**Figure 6c**) with a smaller particle size (13 nm–40 nm). The corresponding NiO lattice fringe distances were measured to be 0.209 nm, 0.242 nm and 0.238 nm, with crystal plane angles of 55.77 and 126.90º which could be interpreted as the cubic NiO phase, visualized along its $[10\bar{1}]$ zone axis. For the bimetal oxide catalyst of CoNi1@C (**Figure 6b**), a small amount of Ni doping decreases the particle size compared to Co@C and leads to particle sizes similar to Ni@C. The corresponding power spectrum reveals that the selected nanocrystal structure

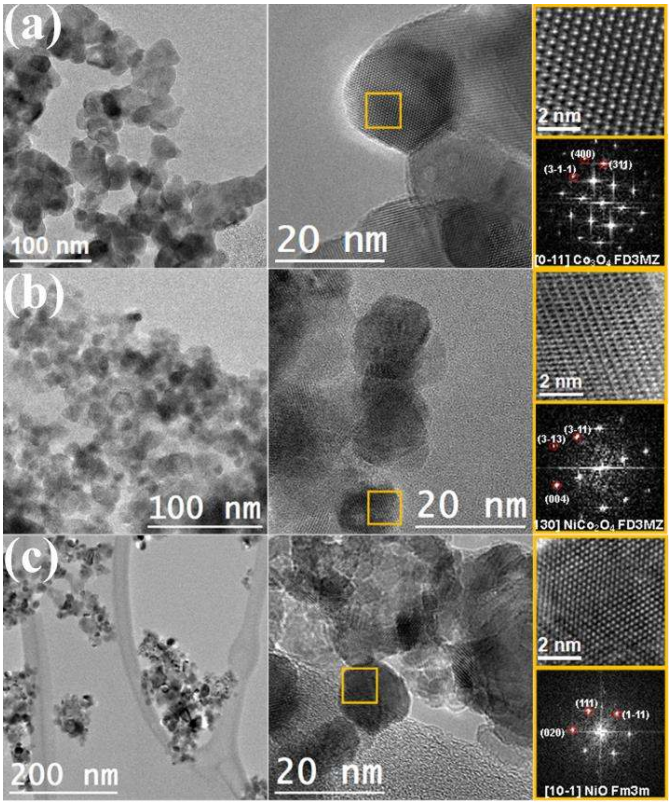


**Figure 6** HRTEM micrographs of the different MOF derived catalysts with corresponding power spectrum of (a) Co@C (b) CoNi1@C and (c) Ni@C.

corresponds to the $NiCo_2O_4$ cubic phase (space group *Fd3mz*) with *a*=*b*=*c*=0.81140 nm, which further confirms the formation of a $Ni_3O_4$–$Co_3O_4$ solid solution. Based on the crystalline domain in **Figure 6b**, the $NiCo_2O_4$ lattice fringe distances were measured to be 0.243 nm, 0.459 nm and 0.233 nm, respectively, at crystal plane angles of 58.37º or 116.59º, which could be attributed to the cubic $NiCo_2O_4$ phase, measured to be 0.243 nm, 0.459 nm and 0.233 nm, respectively, at crystal plane angles of 58.37º or 116.59º, which could be attributed to the cubic $NiCo_2O_4$ phase, visualized along its $[\bar{2}11]$ zone axis. On the other hand, it is difficult to distinguish the mixed phase for CoNi2@C and CoNi3@C due to the uniform overlap. Nevertheless, all these

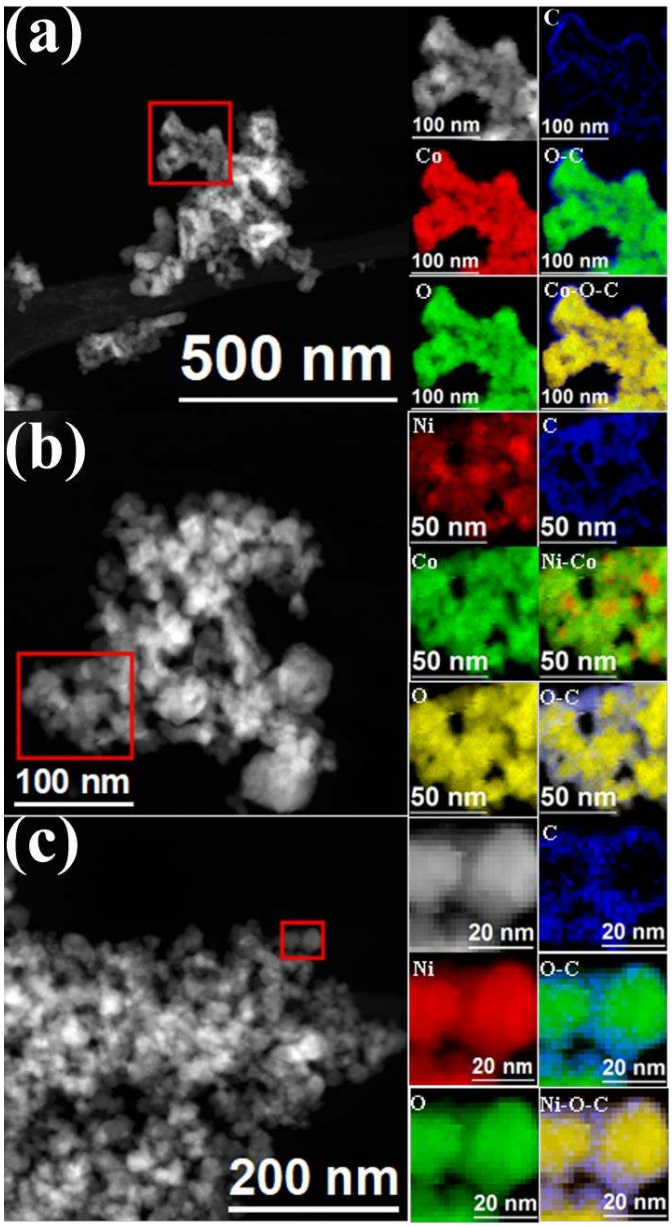


**Figure 7** EELS chemical composition maps of the different MOF derived catalysts obtained from the red squared area of the STEM micrograph of (a) Co@C (b) CoNi1@C and (c) Ni@C, showing individual Ni $L_{2,3}$-edges at 855 eV, Co $L_{2,3}$-edges at 779 eV, O K-edge at 532 eV and C K-edge at 284 eV as well as the composite (Ni-Co, O-C, Co-O-C and Ni-O-C) elemental mapping of these nanostructures.

results are in excellent agreement with the XRD data. The EELS maps (**Figure 7** and **Figures S12-S13**) further reveal the chemical composition of these nanoparticles. Firstly, the mapping images display the existence of M (Co or Ni), O and C elements in these nanoparticles derived from different MOF samples. The elemental maps clearly confirm that C is mainly concentrated on the exterior of the nanostructures for all samples, suggesting the formation of a core-shell structure. These metal oxide particles are connected together by a carbon net, which could impart a high electronic conductivity to the catalyst. Moreover, the mapping images display the uniform distribution of Ni and Co for CoNi3@C (**Figure S12**). Surprisingly, CoNi1@C and, in particular, CoNi2@C show an uneven distribution of Ni and Co as determined from the Ni-Co elemental mapping (**Figure 7** and **Figure S13**), which could be caused by the different diffusion coefficients of Co and Ni in the Ni-Co system during pyrolysis. A similar phenomenon has been discussed in detail by Han et al.[54]

To explore the porous structure of the resulting catalyst, the nitrogen adsorption and desorption isotherms and pore size distributions (based on density functional theory method with slit pore model) of the different catalysts are measured (**Figures S14**). All the adsorption-desorption isotherms exhibit a typical type II curve with a small H3 hysteresis loop in the $P/P_0$ range of 0.8–1.0, indicating the co-existence of large mesopores and small macropores. The BET specific surface areas of Co@C, CoNi1@C, CoNi2@C, CoNi3@C and Ni@C samples are found to be 22.5, 33.7, 29.0, 28.9 and 36.6 $m^2\ g^{-1}$, respectively. With a small amount of Ni doping, the specific surface areas of CoNi1@C increases considerably compared to pure Co-MOF derived materials, which is attributed to the decrease of particle size as proved by TEM results. The pore-size distribution of CoNi2@C, CoNi3@C and Ni@C ranges from 40 nm to more than 100 nm, which is dominated by small macropores. Co@C and CoNi1@C display a broader pore-size distribution with smaller pore sizes and more mesopores, which range from 20 to more than 100 nm. These hierarchical porous structures would be beneficial for the transport of electrolyte ions onto the surface of the active material and facilitate gas bubble dissipation ability.[55-59]

Electrochemical water splitting is a promising strategy for renewable energy conversion and storage, which combines OER and hydrogen evolution reaction (HER). However, the sluggish nature of the OER greatly impedes large-scale applications of electrochemical water splitting. Therefore, the catalytic performance of the as-prepared catalysts for OER was explored by linear sweep voltammetry (LSV) (**Figure 8**). The precious metal catalyst $IrO_2$ was also tested as a comparison under the same conditions. Compared to bare glassy carbon electrode (GCE), all catalysts show obvious catalytic activity for OER. The on-set overpotentials of different catalysts were 0.309 V, 0.263 V, 0.283 V, 0.293 V, 0.298 V and 0.270 V for Co@C, CoNi1@C, CoNi2@C, CoNi3@C, Ni@C and $IrO_2$ catalysts, respectively (**Figure 8**). Among these catalysts, CoNi1@C and $IrO_2$ have the lowest on-set overpotentials. The

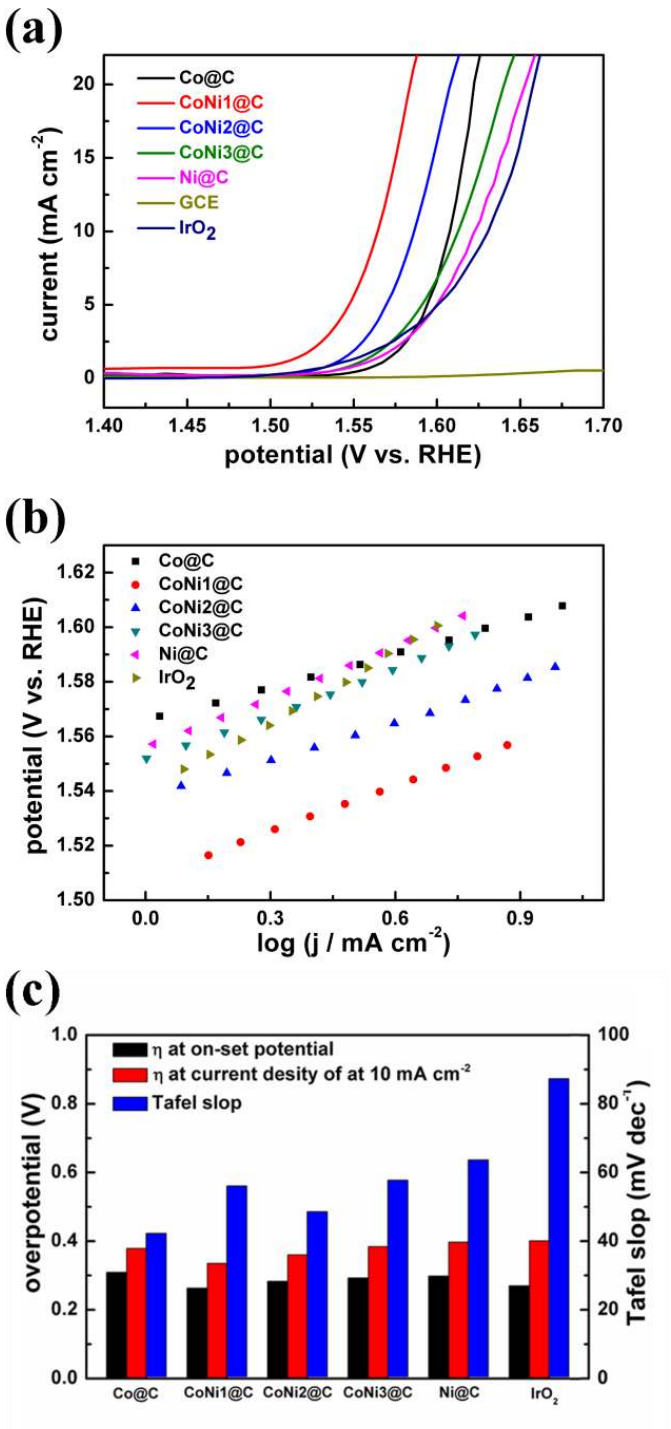


**Figure 8** (a) OER polarization curves using Co@C, CoNi1@C, CoNi2@C, CoNi3@C, Ni@C, or IrO2 catalysts covered GCE and bare GCE at a rotating speed of 1600 rpm in 1 M KOH; (b) Corresponding Tafel plots obtained from respective polarization curves; (c) Comparison of the on-set overpotentials, overpotentials at a current density of 10 mA cm−2 and Tafel slopes of various catalysts. All potentials are against the RHE.

OER kinetics of the catalysts was estimated from Tafel plots. A smaller Tafel slope indicates more favorable OER kinetics of the catalysts. The Tafel plots corresponding to Figure 8a are shown in Figure 8b. The Tafel slopes of Co@C, CoNi1@C, CoNi2@C, CoNi3@C, Ni@C and $IrO_2$ catalysts are 41.8, 55.6, 48.1, 57.3, 63.2 and 86.8 mV $dec^{-1}$, respectively, indicating that the OER was kinetically faster on the MOF-derived catalysts, especially for the Co@C catalyst. The overpotential at a current density of 10 mA $cm^{-2}$ is chosen as another key parameter to evaluate the activity of OER catalysts because this current density matches that of a solar water-splitting device with 12.3% efficiency.[60] Even though $IrO_2$ has a low on-set overpotential, it has the highest overpotential (0.401 V) at a current density of 10 mA $cm^{-2}$ because of the high Tafel slope. Among all the MOF-derived catalysts, CoNi1@C shows the lowest overpotential (0.335 V) at a current density of 10 mA $cm^{-2}$, which is attributed to the combination of low on-set overpotential and low Tafel slope.

The electrochemical impedance spectroscopy (EIS) data are recorded in the frequency range from 100 kHz to 0.1 Hz at $\eta$ = 380 mV with an amplitude of 5 mV, where Z' and Z'' are the real and imaginary parts of the impedance, respectively. The data was fitted adequately by a modified Randles' equivalent circuit shown in the inset of **Figure S15**. The intersection of the plots on the real axis in the higher frequency region represents the equivalent series resistance ($R_s$), which includes the electrolyte resistance, the contact resistance and the intrinsic resistance of the electrode. The diameter of the semi-circle represents the charge transfer resistance ($R_{ct}$). A lower $R_{ct}$ corresponds to a faster charge transfer process.[61, 62] Using the equivalent circuit as shown in **Figure S15**, the fitting results for EIS measurements of different catalysts are obtained (**Table S2**). Among these catalysts, CoNi1@C exhibited the lowest $R_{ct}$ resistance (3.4 Ω), implying its fast charge transfer process and thus favorable electrocatalytic activity for OER.

In order to increase the surface area of the electrode, nickel foam was chosen as a substrate to load the catalysts in a three-electrode system for electrochemical polarization studies (**Figure 9a**). Both $IrO_2$ and CoNi1@C exhibit a significant enhancement of OER catalytic performance compared to GC based samples. Particularly, CoNi1@C displays an overpotential of as low as 276 mV on Ni foam at a current density of 10 mA $cm^{-2}$ (**Figure 9a** and **Table S3**), which is higher than state-of-the-art Co-Ni mixed oxide catalysts derived from MOFs for OER. At an overpotential of 400 mV (*i.e.* at a potential of 1.63V *vs*. RHE), the current density of CoNi1@C covered electrode (197 mA $cm^{-2}$) is 3.6 times that of the $IrO_2$ covered electrode (55 mA $cm^{-2}$) (**Figure 9a**).

In addition, a higher pyrolysis temperature has been explored for CoNi1@C. With the increase of temperature, the catalytic performance for OER slightly decreased due to the decrease of surface area (**Figure S16**), which could be caused by the increase of particle size with a higher pyrolysis temperature.[63] These results are in agreement with previous studies for MOF-derived materials.[64-66] Chronopotentiometric curves of CoNi1@C at different current densities (from 10 to 100 mA $cm^{-2}$) and chronopotentiometric durability tests at a constant current density of 20 mA $cm^{-2}$ were recorded (**Figure 9b**). CoNi1@C exhibits excellent durability at large current densities (*e.g.* 100 mA $cm^{-2}$) over a long time (*e.g.* 48 h), which could be associated with the thin carbon shell of the CoNi1@C catalyst. Obviously, the high catalytic activity of CoNi1@C for OER is promising for electrochemical water splitting.

Furthermore, while Pt/C catalyst still greatly surpasses all other kinds of catalysts for HER, in this study, Pt/C catalyst and CoNi1@C catalyst were chosen as the catalysts for the cathode

and the anode, respectively, to establish a single electrolyzer cell. At current densities of 10, 20 and 50 mA $cm^{-2}$, the cell voltages are 1.53 V, 1.58 V and 1.66 V, respectively (**Figure 9c**). In addition, the electrolyzer based on Pt/C catalyst and CoNi1@C catalyst exhibits excellent stability over 48 h during the electrolysis tests (**Figure 9d**).

After stability test, the chemical composition and morphology are explored *via* TEM and EELS mapping. Compared with the catalyst of CoNi1@C before test, no distinct change in the morphology can be observed, which could benefit from a carbon shell network of CoNi1@C. **Figure S17** shows the EELS chemical composition maps obtained from the red squared region in the HAADF STEM micrograph. As can be seen in the maps, the region of interest contains information about a few nanostructures. Firstly, the mapping images display the existence of Ni, Co, O and C in the nanostructures present in the sample. There are no other possible contamination elements that can be detected. Then the same results of metal elements are further confirmed by WDS (detection limit can reach ppm level and around 0.05 wt%)[67] as shown in **Figure S18**. However, the increase of Ni can be clearly observed, compared with CoNi1@C before test, which is probably come from anodic dissolution of Ni foam. In order to prove this hypothesis, the same stability test was carried out by the substrate of carbon paper. After stability test, CoNi1@C on the carbon paper exhibited lower Ni content (24.6 at.%) than on the Ni foam (32.9%), confirmed by WDS (**Table S3**).

The catalyst performance of the CoNi1@C catalyst for OER not only surpasses bimetallic MOFs of PBA[21], MOF-74[22] or partially doped ZIF-67(Co-Ni)[68] derived Co-Ni mixed oxide catalysts, but also outperforms most Co-Ni based catalysts developed via other methods (**Table S4**). Compared with some state-of-the-art seamless integration electrodes with Ni foam as the substrate,[69-71] CoNi1@C exhibits a slightly higher overpotential at the high current density of 100 mA $cm^{-2}$, which is probably caused by the addition of binder during our coating procedure.

The high OER catalyst activity of CoNi1@C could be attributed to the following reasons: (1) the synergistic effect of bimetal oxides. More importantly, the stabilized high valence state of Ni, which is regarded as the real active site, could promote the OER. In the spinel structure, the trivalent ions play an important role in stimulating the absorbed oxygen by the beneficial electrostatic adsorption of $OH^-$ ions to the formation of MOOH and then inducing deprotonation of $OOH^-$ species to produce $O_2$.[72-75] (2) This unique structure of hierarchical porous honeycomb-like structure could facilitate the transportation of electrolyte ions and enhance the stability of the structure during the electrochemical test.[76-78]

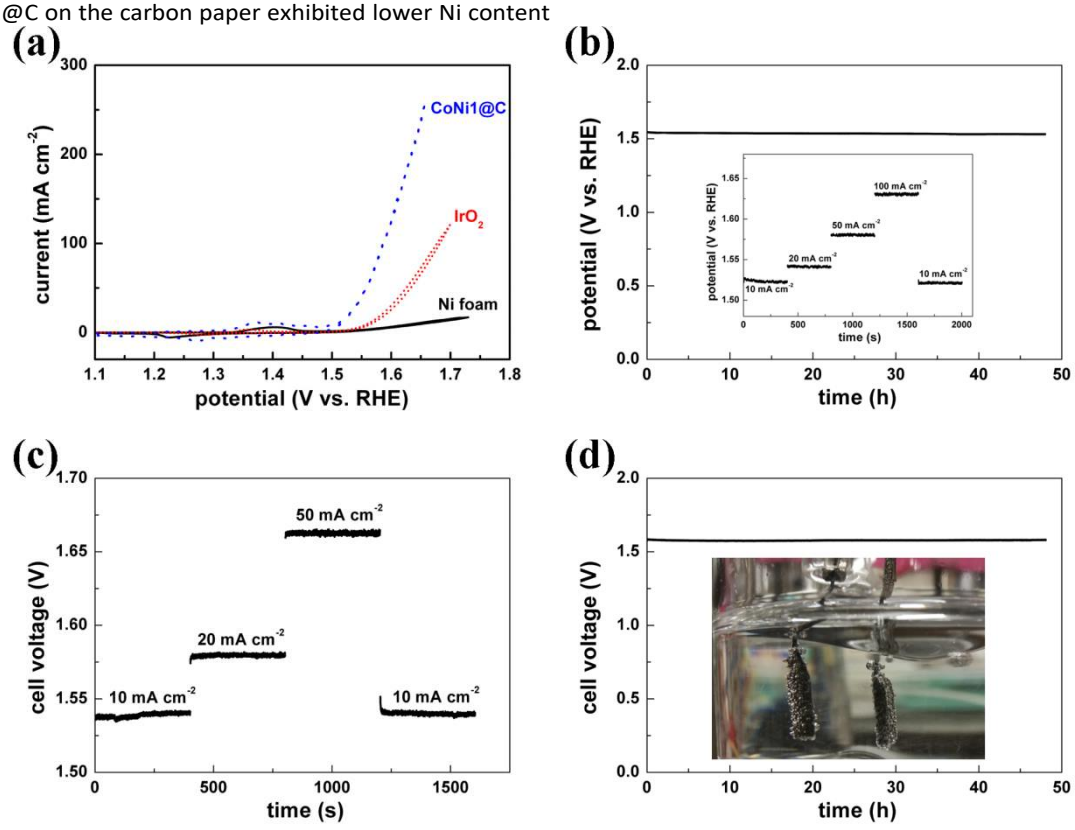


**Figure 9** (a) OER polarization curves of CoNi1@C, $IrO_2$ catalysts covered Ni foam and bare Ni foam in 1 M KOH in a three-electrode system; (b) Multi-current process of CoNi1@C covered Ni foam at different constant current densities and durability test at a constant current density of 20 mA $cm^{-2}$ in a three-electrode system; (c) Multi-current process in a two-electrode configuration as a single electrolyzer cell, using CoNi1@C as catalyst for OER and Pt/C for HER in 1 M KOH. Support: Ni foam; loading of catalyst: 3 mg $cm^{-2}$. (d) Durability test at a constant current density of 20 mA $cm^{-2}$ for the single electrolyzer cell over 48 h. Inset shows a photograph of the electrolyzer cell system during water electrolysis in 1 M KOH to generate oxygen gas (left) and hydrogen gas (right).

Journal of Materials Chemistry A

ARTICLE

In addition, a carbon shell network could ensure the electrical continuity of bimetal oxide particles and suppress the agglomeration of nanoparticles during pyrolysis and electrochemical tests.

## 3. Conclusions

In summary, a new series of bimetallic MOFs were successfully prepared using the one-step synthesis method. The molar ratio of the metal nodes in these bimetallic MOFs can be arbitrarily varied while the nodes are randomly and uniformly distributed inside the frameworks. Moreover, the pillars in this series of bimetallic MOFs are tunable. As expected, with incorporation of a second metal ion, intrinsic properties (such as thermal stabilities and band gap) of the pristine MOFs can be tailored. In order to prepare bimetal oxide catalysts for OER, these bimetallic MOFs were pyrolized and used as self-sacrificial templates. The resulting materials showed a hierarchical porous honeycomb-like structure of carbon covered (bi)metal oxide nanostructure. After pyrolysis, the bimetallic MOF with a high ratio of Co leads to the highest catalyst performance for OER due to the unique structure and high valence state of Ni. At a current density of 10 mA $cm^{-2}$, the overpotentials of CoNi1@C are 335 mV and 276 mV for OER on RDE and Ni foam, respectively. These promising results not only prove that the properties of MOFs can be tailored by incorporation of a second metal into the MOF structure but also show possibilities for wider applications of this new bimetallic MOF family.

## 4. Experimental

### 4.1 Preparation of bimetallic MOFs

All the chemicals were used without further purification. In a typical method, different proportions of $Co(NO_3)_2{\cdot}6H_2O$ (≥99%, Merck, Germany) and $Ni(NO_3)_2{\cdot}6H_2O$ (≥99%, VWR International bvba, Belgium) were dissolved in 40 ml N,N-dimethylformamide (DMF, ≥99% Chem-Lab). 1,3,5-benzenetricarboxylic acid (0.844 g, $H_3BTC$, 98% purity, ABCR, Germany) and 4,4-dipyridyl (0.768 g bipy, 98% purity, Acros Organics) were dissolved in 40 ml DMF as well. The two homogeneous solutions were mixed together into a 100 mL glass bottle. The molar ratios of $Co(NO_3)_2{\cdot}6H_2O$ *vs.* $Ni(NO_3)_2{\cdot}6H_2O$ are shown in **Figure S19** while the total molar concentration of metal salts is 12 mmol. After that, the glass bottle was maintained at 50 °C in a water bath (Memmert, WNB 45) for 72 h and then naturally cooled down to room temperature. In order to remove the residual reactant, the powder was washed several times with DMF and ethanol successively. The corresponding samples from pure cobalt-MOF to pure nickel-MOF were denoted as Co-MOF, CoNiBMMOF-1, CoNiBMMOF-2, CoNiBMMOF-3, CoNiBMMOF-4, CoNiBMMOF-5, and Ni-MOF, respectively. In order to prove that new families of bimetallic MOFs can be tailored by the pillar strategy, an identical series of bimetallic MOFs based on DMF as the pillar were prepared by the same method at 100 °C. The details are shown in **Table S5**.

### 4.2 Preparation of MOF derived bimetallic catalysts

The Co-MOF, CoNiBMMOF-1, CoNiBMMOF-2, CoNiBMMOF-3 and Ni-MOF were pyrolyzed at 500 °C for 8 h in a nitrogen gas atmosphere with a flow rate of 300 mL $min^{-1}$. The temperature inside the furnace was gradually increased to 500 °C at a heating rate of 3 °C $min^{-1}$. After the pyrolysis, the furnace was cooled down to room temperature with a cooling rate of 3 °C $min^{-1}$. The resulting powder was ultrasonically cleaned with DI water and EtOH successively, and then dried at 60 °C. After that, the as-prepared black powder was further annealed at 350 °C for 3 h with a heating rate of 3 °C $min^{-1}$ in air to oxidize the metal phase. The different kinds of MOF-derived catalysts were denoted as Co@C, CoNi1@C, CoNi2@C, CoNi3@C and Ni@C, respectively.

### 4.3 Material characterizations

Thermogravimetric analysis (TGA) was performed on a thermogravimetric analyzer (AutoTGA 2950HR V5.4A, TA Instruments) using platinum pans at a heating rate of 5 °C $min^{-1}$ in $N_2$ atmosphere. Decomposition temperatures are deduced by intersection of a straight baseline with the tangent of the weight versus temperature. A Bruker AXS D8 diffractometer (Cu Kα radiation with $\lambda$ = 0.15405 nm and Ni filter) with $2\vartheta$ ranging from 5° to 30° and a step of 0.02° (2 s per step) was used to record X-ray diffraction (XRD) patterns of all samples. The morphologies and structures of samples were observed on a FEI/Philips XL30 FEG microscope (SEM). Metal compositional analyses of BMMOFs were determined by full quantitative electron probe micro-analyzer system coupled with wavelength dispersive spectroscopy (EPMA-WDS; JEOL JXA-8530F, Tokyo, Japan) with an acceleration voltage of 15 kV at a probe current of 15 nA. Before SEM and EPMA test, BMMOFs were sputtered with a 10 nm layer of Pt to improve the electronic conductivity. Scanning Transmission Electron Microscopy (STEM) and High Resolution Transmission Electron Microscopy (HRTEM) images were collected using an FEI Tecnai F20 field emission gun microscope operated at 200 kV

with a point-to-point resolution of 0.19 nm, which is equipped with high angle annular dark field (HAADF) and electron energy loss spectroscopy (EELS) detectors. The obtained images and spectra were analyzed by Gatan Digital Micrograph software. ESCALAB250 (monochromatic Al Kα with 1486.6 eV) was used to collect X-ray photoelectron spectroscopy (XPS) data. The metal compositions in Co-MOF, Ni-MOF and BMMOFs (dissolved in 0.5M HCL) were analyzed by inductively coupled plasma optical emission spectroscopy (ICP-OES, Varian 720-ES). A micromeritics ASAP 2020 apparatus was used to investigate the specific surface area and pore size distributions. Diffuse reflectance UV-Vis-NIR spectroscopy was carried out on a Varian Cary 5000 UV–Vis–NIR spectrophotometer at room temperature.

#### 4.4 Electrochemical characterizations:

**Preparation of working electrodes.** The catalysts inks were prepared by dispersing 10 mg catalyst into 1 mL solvent (800 µL ethanol and 200 µL DI water) containing 20 µL 5 wt% Nafion (Alfa Aesar Germany). Before loading the catalysts on the GCE, the ink was sonicated for 30 minutes. Then 10 µL as-prepared catalyst ink was loaded on the surface of the GCE (5 mm in diameter) corresponding to an aerial mass loading of about 0.50 mg $cm^{-2}$. For comparison, $IrO_2$ (P40V020, particles from Premetek Co.) were used in identical electrochemical tests with the same mass loading. Electrochemical water splitting was carried out with Pt/C catalyst (10% of platinum, Alfa Aesar Germany) and bimetallic MOFs derived catalyst as cathode and anode, respectively. Ni foam electrodes were prepared using the same procedure with catalysts aerial mass loading of around 3.0 mg $cm^{-2}$ based on the geometrical area for both Pt/C catalyst and bimetallic MOF derived catalyst.

**Catalytic performance.** The OER catalytic performance of the samples was evaluated by linear sweep voltammetry (LSV) technique using an Autolab electrochemical workstation at room temperature. The tests are carried out in a three-electrode cell using a rotating disk electrode (RDE, PINE Research Company) at a rotation speed of 1600 rpm or without rotation. The glassy carbon electrode (GCE) or Ni foam, a Hg/HgO electrode and a graphite plate (1 cm × 5 cm) were used as the working electrode, the reference electrode and the counter electrode, respectively. Prior to the measurement, the electrolyte was purged with $O_2$ for at least 30 min. The electrolyte was continuously bubbled with $O_2$ during all the tests. The supporting electrolyte was 1 M KOH for all tests. The LSV currents are normalized by the mass of the active materials and the geometrical area of the GCE or the Ni foam respectively. All potentials were converted to the reversible hydrogen electrode (RHE) potential as follows:

$$E_{\mathrm{RHE}} = E_{\mathrm{Hg/HgO}} + 0.098 + 0.059 \times \mathrm{pH}$$

All LSV curves were *iR*-corrected to compensate the influence of the solution resistance by the following equation:

$$E_{\mathrm{iR-corrected}} = E - iR$$

where $i$ is the current (A) and $R$ (Ω) is the electrolyte resistance measured by electrochemical impedance spectroscopy (EIS).

## Conflicts of interest

There are no conflicts to declare

## Acknowledgements

X. Zhang is grateful to China Scholarship Council. J. Luo acknowledges the Research Foundation – Flanders (FWO) for a Research Project (G0B3218N), Research Grant (1529816N) and a travel grant (V410316N) for a Visiting Professorship at the Technical University of Denmark. TZ, PYT and JA acknowledge funding from Generalitat de Catalunya 2017 SGR 327 and the Spanish MINECO project VALPEC (ENE2017-85087-C3). ICN2 acknowledges support from the Severo Ochoa Programme (MINECO, Grant no. SEV-2017-0706) and is funded by the CERCA Programme / Generalitat de Catalunya. Part of the present work has been performed in the framework of Universitat Autònoma de Barcelona Materials Science PhD program. TZ has received funding from the CSC-UAB PhD scholarship program. D.P. acknowledges the Research Foundation – Flanders (FWO) for Ph.D. (aspirant) Fellowship. We thank Iris Cuppens and Dr. Fei Wang (Department of Materials Engineering, KU Leuven) for the assistance of EPMA and ICP measurements. Funding from the National Natural Science Foundation of China (No. 21776120), "Minjiang Scholar" Program and key project (No. JZ160480) of Department of Education, Fujian Province, China, and Open Project (No. 201607) of State Key Laboratory of Physical Chemistry of Solid Surfaces, Xiamen University is also acknowledged.

## Notes and references

1. H. Furukawa, K. E. Cordova, M. O'Keeffe and O. M. Yaghi, The chemistry and applications of metal-organic frameworks. *Science* **2013,** *341* (6149), 1230444.
2. K. Shen, X. Chen, J. Chen and Y. Li, Development of MOF-Derived Carbon-Based Nanomaterials for Efficient Catalysis. *ACS Catalysis* **2016,** *6* (9), 5887-5903.
3. W. Xia, A. Mahmood, R. Zou and Q. Xu, Metal–organic frameworks and their derived nanostructures for electrochemical energy storage and conversion. *Energy & Environmental Science* **2015,** *8* (7), 1837-1866.
4. X. Zhang, J. Luo, P. Tang, X. Ye, X. Peng, H. Tang, S.-G. Sun and J. Fransaer, A universal strategy for metal oxide anchored and binder-free carbon matrix electrode: A supercapacitor case with superior rate performance and high mass loading. *Nano Energy* **2017,** *31*, 311-321.
5. X. Yang and Q. Xu, Bimetallic Metal–Organic Frameworks for Gas Storage and Separation. *Crystal Growth & Design* **2017,** *17* (4), 1450-1455.
6. J. A. Botas, G. Calleja, M. Sánchez-Sánchez and M. G. Orcajo, Effect of Zn/Co ratio in MOF-74 type materials

 

containing exposed metal sites on their hydrogen adsorption behaviour and on their band gap energy. *International Journal of Hydrogen Energy* **2011,** *36* (17), 10834-10844.

7. D. Kim and A. Coskun, Template-Directed Approach Towards the Realization of Ordered Heterogeneity in Bimetallic Metal-Organic Frameworks. *Angewandte Chemie* **2017,** *56* (18), 5071-5076.
8. D. Sun, F. Sun, X. Deng and Z. Li, Mixed-Metal Strategy on Metal-Organic Frameworks (MOFs) for Functionalities Expansion: Co Substitution Induces Aerobic Oxidation of Cyclohexene over Inactive Ni-MOF-74. *Inorganic chemistry* **2015,** *54* (17), 8639-8643.
9. J. A. Villajos, G. Orcajo, C. Martos, J. Á. Botas, J. Villacañas and G. Calleja, Co/Ni mixed-metal sited MOF-74 material as hydrogen adsorbent. *International Journal of Hydrogen Energy* **2015,** *40* (15), 5346-5352.
10. E. A. Dolgopolova, A. J. Brandt, O. A. Ejegbavwo, A. S. Duke, T. D. Maddumapatabandi, R. P. Galhenage, B. W. Larson, O. G. Reid, S. C. Ammal, A. Heyden, M. Chandrashekhar, V. Stavila, D. A. Chen and N. B. Shustova, Electronic Properties of Bimetallic Metal-Organic Frameworks (MOFs): Tailoring the Density of Electronic States through MOF Modularity. *Journal of the American Chemical Society* **2017**.
11. M. Cheng, Y. S. Ding, E. Q. Gao, Z. Zhang and Q. X. Jia, Composition dependence of magnetic relaxation for CoNi chain-based compounds with mixed double azide-tetrazolate bridges. *Dalton transactions* **2016,** *45* (19), 8028-8035.
12. B. Dhara, V. Kumar, K. Gupta, P. K. Jha and N. Ballav, Giant Enhancement of Carrier Mobility in Bimetallic Coordination Polymers. *ACS Omega* **2017,** *2* (8), 4488-4493.
13. M. Lammert, C. Glissmann and N. Stock, Tuning the stability of bimetallic Ce(iv)/Zr(iv)-based MOFs with UiO-66 and MOF-808 structures. *Dalton transactions* **2017,** *46* (8), 2425-2429.
14. X. Song, M. Oh and M. S. Lah, Hybrid bimetallic metal-organic frameworks: modulation of the framework stability and ultralarge CO2 uptake capacity. *Inorganic chemistry* **2013,** *52* (19), 10869-10876.
15. Y. Q. Wang, A. L. Cheng, P. P. Liu and E. Q. Gao, Unusual composition dependence of magnetic relaxation for Co(II)(1-x)Ni(II)(x) chain-based metal-organic frameworks. *Chemical communications* **2013,** *49* (62), 6995-6997.
16. H. Xu, C. S. Cao, X. M. Kang and B. Zhao, Lanthanide-based metal-organic frameworks as luminescent probes. *Dalton transactions* **2016,** *45* (45), 18003-18017.
17. Q. Zhang, B. Li and L. Chen, First-principles study of microporous magnets M-MOF-74 (M = Ni, Co, Fe, Mn): the role of metal centers. *Inorganic chemistry* **2013,** *52* (16), 9356-9362.
18. W. Zhang, Y. Shi, C. Li, Q. Zhao and X. Li, Synthesis of Bimetallic MOFs MIL-100(Fe-Mn) as an Efficient Catalyst for Selective Catalytic Reduction of NO x with NH3. *Catalysis Letters* **2016,** *146* (10), 1956-1964.
19. J. Zhou, H. Li, H. Zhang, H. Li, W. Shi and P. Cheng, A Bimetallic Lanthanide Metal-Organic Material as a Self-Calibrating Color-Gradient Luminescent Sensor. *Advanced materials* **2015,** *27* (44), 7072-7077.
20. F. Zou, X. Hu, Z. Li, L. Qie, C. Hu, R. Zeng, Y. Jiang and Y. Huang, MOF-derived porous ZnO/ZnFe(2)O(4)/C octahedra with hollow interiors for high-rate lithium-ion batteries. *Advanced materials* **2014,** *26* (38), 6622-6628.
21. L. Han, X. Y. Yu and X. W. Lou, Formation of Prussian-Blue-Analog Nanocages via a Direct Etching Method and their Conversion into Ni-Co-Mixed Oxide for Enhanced Oxygen Evolution. *Advanced materials* **2016,** *28* (23), 4601-4605.
22. D. Sun, L. Ye, F. Sun, H. Garcia and Z. Li, From Mixed-Metal MOFs to Carbon-Coated Core-Shell Metal Alloy@Metal Oxide Solid Solutions: Transformation of Co/Ni-MOF-74 to CoxNi1-x@CoyNi1-yO@C for the Oxygen Evolution Reaction. *Inorganic chemistry* **2017,** *56* (9), 5203-5209.
23. A. B. Soliman, M. H. Hassan, A. A. Abugable, S. G. Karakalos and M. H. Alkordi, Post‐Synthetic Immobilization of Ni Ions in a Porous‐Organic Polymer‐Graphene Composite for Non‐Noble Metal Electrocatalytic Water Oxidation. *ChemCatChem* **2017,** *9* (15), 2946-2951.
24. W. Cho, Y. H. Lee, H. J. Lee and M. Oh, Multi ball-in-ball hybrid metal oxides. *Advanced materials* **2011,** *23* (15), 1720-1723.
25. X. Ge, Z. Li, C. Wang and L. Yin, Metal-Organic Frameworks Derived Porous Core/Shell Structured ZnO/ZnCo2O4/C Hybrids as Anodes for High-Performance Lithium-Ion Battery. *ACS applied materials & interfaces* **2015,** *7* (48), 26633-26642.
26. W. Guo, W. Sun and Y. Wang, Multilayer CuO@ NiO hollow spheres: microwave-assisted metal–organic-framework derivation and highly reversible structure-matched stepwise lithium storage. *ACS nano* **2015,** *9* (11), 11462-11471.
27. G. Huang, L. Zhang, F. Zhang and L. Wang, Metal-organic framework derived Fe2O3@NiCo2O4 porous nanocages as anode materials for Li-ion batteries. *Nanoscale* **2014,** *6* (10), 5509-5515.
28. X. Xu, Z. Zhang and X. Wang, Well-Defined Metal-Organic-Framework Hollow Nanostructures for Catalytic Reactions Involving Gases. *Advanced materials* **2015,** *27* (36), 5365-5371.
29. D. Yu, B. Wu, L. Ge, L. Wu, H. Wang and T. Xu, Decorating nanoporous ZIF-67-derived NiCo2O4 shells on a Co3O4 nanowire array core for battery-type electrodes with enhanced energy storage performance. *Journal of Materials Chemistry A* **2016,** *4* (28), 10878-10884.
30. Y. Zhao, X. Li, J. Liu, C. Wang, Y. Zhao and G. Yue, MOF-Derived ZnO/Ni3ZnC0.7/C Hybrids Yolk-Shell Microspheres with Excellent Electrochemical Performances for Lithium Ion Batteries. *ACS applied materials & interfaces* **2016,** *8* (10), 6472-6480.
31. W. R. Lee, D. W. Ryu, W. J. Phang, J. H. Park and C. S. Hong, Charge effect of foreign metal ions and the crystal growth process in hybridized metal-organic frameworks. *Chemical communications* **2012,** *48* (88), 10847-10849.
32. L. Zhang and Y. H. Hu, Strong Effects of Higher-Valent Cations on the Structure of the Zeolitic Zn(2-methylimidazole)2 Framework (ZIF-8). *The Journal of Physical Chemistry C* **2011,** *115* (16), 7967-7971.
33. J. A. Botas, G. Calleja, M. Sanchez-Sanchez and M. G. Orcajo, Cobalt doping of the MOF-5 framework and its effect on gas-adsorption properties. *Langmuir : the ACS journal of surfaces and colloids* **2010,** *26* (8), 5300-5303.
34. B. Chen, G. Ma, Y. Zhu, J. Wang, W. Xiong and Y. Xia, Metal-

organic-framework-derived bi-metallic sulfide on N, S-codoped porous carbon nanocomposites as multifunctional electrocatalysts. *Journal of Power Sources* **2016,** *334*, 112-119.

35. M. A. Gotthardt, R. Schoch, S. Wolf, M. Bauer and W. Kleist, Synthesis and characterization of bimetallic metal-organic framework Cu-Ru-BTC with HKUST-1 structure. *Dalton transactions* **2015,** *44* (5), 2052-2056.
36. W. Guo, W. Xia, K. Cai, Y. Wu, B. Qiu, Z. Liang, C. Qu and R. Zou, Kinetic-Controlled Formation of Bimetallic Metal-Organic Framework Hybrid Structures. *Small* **2017,** *13* (41).
37. A. Schejn, A. Aboulaich, L. Balan, V. Falk, J. Lalevée, G. Medjahdi, L. Aranda, K. Mozet and R. Schneider, Cu2+-doped zeolitic imidazolate frameworks (ZIF-8): efficient and stable catalysts for cycloadditions and condensation reactions. *Catalysis Science & Technology* **2015,** *5* (3), 1829-1839.
38. H. Yang, X.-W. He, F. Wang, Y. Kang and J. Zhang, Doping copper into ZIF-67 for enhancing gas uptake capacity and visible-light-driven photocatalytic degradation of organic dye. *Journal of Materials Chemistry* **2012,** *22* (41), 21849.
39. J. Chen, S. Li, V. Kumar and P. S. Lee, Carbon Coated Bimetallic Sulfide Hollow Nanocubes as Advanced Sodium Ion Battery Anode. *Advanced Energy Materials* **2017,** *7* (19), 1700180.
40. L. Du, L. Luo, Z. Feng, M. Engelhard, X. Xie, B. Han, J. Sun, J. Zhang, G. Yin, C. Wang, Y. Wang and Y. Shao, Nitrogen–doped graphitized carbon shell encapsulated NiFe nanoparticles: A highly durable oxygen evolution catalyst. *Nano Energy* **2017,** *39*, 245-252.
41. L. Ma, T. Chen, G. Zhu, Y. Hu, H. Lu, R. Chen, J. Liang, Z. Tie, Z. Jin and J. Liu, Pitaya-like microspheres derived from Prussian blue analogues as ultralong-life anodes for lithium storage. *Journal of Materials Chemistry A* **2016,** *4* (39), 15041-15048.
42. M. Okubo, D. Asakura, Y. Mizuno, T. Kudo, H. Zhou, A. Okazawa, N. Kojima, K. Ikedo, T. Mizokawa and I. Honma, Ion-induced transformation of magnetism in a bimetallic CuFe Prussian blue analogue. *Angewandte Chemie* **2011,** *50* (28), 6269-6273.
43. D. Wang, X. Qi, H. Gao, J. Yu, Y. Zhao, G. Zhou and G. Li, Fabricating hierarchical porous ZnCo 2 O 4 microspheres as high-performance anode material for lithium-ion batteries. *Materials Letters* **2016,** *164*, 93-96.
44. L. Yan, Y. Liu, K. Zha, H. Li, L. Shi and D. Zhang, Scale-Activity Relationship of MnOx-FeOy Nanocage Catalysts Derived from Prussian Blue Analogues for Low-Temperature NO Reduction: Experimental and DFT Studies. *ACS applied materials & interfaces* **2017,** *9* (3), 2581-2593.
45. L. Zhang, L. Shi, L. Huang, J. Zhang, R. Gao and D. Zhang, Rational Design of High-Performance DeNOx Catalysts Based on MnxCo3–xO4 Nanocages Derived from Metal–Organic Frameworks. *ACS Catalysis* **2014,** *4* (6), 1753-1763.
46. H.-H. Zou, C.-Z. Yuan, H.-Y. Zou, T.-Y. Cheang, S.-J. Zhao, U. Y. Qazi, S.-L. Zhong, L. Wang and A.-W. Xu, Bimetallic phosphide hollow nanocubes derived from a prussian-blue-analog used as high-performance catalysts for the oxygen evolution reaction. *Catalysis Science & Technology* **2017,** *7* (7), 1549-1555.
47. Y. Jiao, C. R. Morelock, N. C. Burtch, W. P. Mounfield, J. T. Hungerford and K. S. Walton, Tuning the Kinetic Water Stability and Adsorption Interactions of Mg-MOF-74 by Partial Substitution with Co or Ni. *Industrial & Engineering Chemistry Research* **2015,** *54* (49), 12408-12414.
48. H. Deng, S. Grunder, K. E. Cordova, C. Valente, H. Furukawa, M. Hmadeh, F. Gándara, A. C. Whalley, Z. Liu and S. Asahina, Large-pore apertures in a series of metal-organic frameworks. *Science* **2012,** *336* (6084), 1018-1023.
49. Y. Li, L. Xie, Y. Liu, R. Yang and X. Li, Favorable hydrogen storage properties of M (HBTC)(4, 4′ -bipy) • 3DMF (M= Ni and Co). *Inorganic chemistry* **2008,** *47* (22), 10372-10377.
50. A. Calderón-Casado, G. Barandika, B. Bazán, M.-K. Urtiaga, O. Vallcorba, J. Rius, C. Miravittles and M.-I. Arriortua, Solid-state transformation of the MOF [Ni2(bipy)1.5(PDC)2(H2O)2]·3.5H2O. *CrystEngComm* **2011,** *13* (22), 6831.
51. E. Gallo, C. Lamberti and P. Glatzel, dd excitations in CPO-27-Ni metal-organic framework: comparison between resonant inelastic X-ray scattering and UV-vis spectroscopy. *Inorganic chemistry* **2013,** *52* (10), 5633-5635.
52. X. Li, Y. Fang, X. Lin, M. Tian, X. An, Y. Fu, R. Li, J. Jin and J. Ma, MOF derived Co3O4 nanoparticles embedded in N-doped mesoporous carbon layer/MWCNT hybrids: extraordinary bi-functional electrocatalysts for OER and ORR. *Journal of Materials Chemistry A* **2015,** *3* (33), 17392-17402.
53. S. Kuboon and Y. H. Hu, Study of NiO−CoO and Co3O4−Ni3O4Solid Solutions in Multiphase Ni−Co−O Systems. *Industrial & Engineering Chemistry Research* **2011,** *50* (4), 2015-2020.
54. L. Han, Q. Meng, D. Wang, Y. Zhu, J. Wang, X. Du, E. A. Stach and H. L. Xin, Interrogation of bimetallic particle oxidation in three dimensions at the nanoscale. *Nature communications* **2016,** *7*, 13335.
55. S. Chen and S.-Z. Qiao, Hierarchically porous nitrogen-doped graphene–NiCo2O4 hybrid paper as an advanced electrocatalytic water-splitting material. *Acs Nano* **2013,** *7* (11), 10190-10196.
56. X. Gao, H. Zhang, Q. Li, X. Yu, Z. Hong, X. Zhang, C. Liang and Z. Lin, Hierarchical NiCo2O4 Hollow Microcuboids as Bifunctional Electrocatalysts for Overall Water‐Splitting. *Angewandte Chemie* **2016,** *128* (21), 6398-6402.
57. X. Lu and C. Zhao, Electrodeposition of hierarchically structured three-dimensional nickel-iron electrodes for efficient oxygen evolution at high current densities. *Nature communications* **2015,** *6*, 6616.
58. C. Ouyang, X. Wang, C. Wang, X. Zhang, J. Wu, Z. Ma, S. Dou and S. Wang, Hierarchically Porous Ni3S2 Nanorod Array Foam as Highly Efficient Electrocatalyst for Hydrogen Evolution Reaction and Oxygen Evolution Reaction. *Electrochimica Acta* **2015,** *174*, 297-301.
59. C. Xiao, Y. Li, X. Lu and C. Zhao, Bifunctional Porous NiFe/NiCo2O4/Ni Foam Electrodes with Triple Hierarchy and Double Synergies for Efficient Whole Cell Water Splitting. *Advanced Functional Materials* **2016,** *26* (20), 3515-3523.
60. J. Luo, J.-H. Im, M. T. Mayer, M. Schreier, M. K. Nazeeruddin, N.-G. Park, S. D. Tilley, H. J. Fan and M. Grätzel, Water photolysis at 12.3% efficiency via perovskite photovoltaics and Earth-abundant catalysts. *Science* **2014,** *345* (6204), 1593-1596.
61. S.-H. Bae, J.-E. Kim, H. Randriamahazaka, S.-Y. Moon, J.-Y.

 

Park and I.-K. Oh, Seamlessly Conductive 3D Nanoarchitecture of Core-Shell Ni-Co Nanowire Network for Highly Efficient Oxygen Evolution. *Advanced Energy Materials* **2017,** *7* (1), 1601492.

62. Y. Li, L. Hu, W. Zheng, X. Peng, M. Liu, P. K. Chu and L. Y. S. Lee, Ni/Co-based nanosheet arrays for efficient oxygen evolution reaction. *Nano Energy* **2018,** *52*, 360-368.
63. Y. Lu, W. Zhan, Y. He, Y. Wang, X. Kong, Q. Kuang, Z. Xie and L. Zheng, MOF-templated synthesis of porous Co(3)O(4) concave nanocubes with high specific surface area and their gas sensing properties. *ACS applied materials & interfaces* **2014,** *6* (6), 4186-4195.
64. C. Bai, A. Li, X. Yao, H. Liu and Y. Li, Efficient and selective aerobic oxidation of alcohols catalysed by MOF-derived Co catalysts. *Green Chemistry* **2016,** *18* (4), 1061-1069.
65. B. Chen, G. Ma, Y. Zhu and Y. Xia, Metal-organic-frameworks derived cobalt embedded in various carbon structures as bifunctional electrocatalysts for oxygen reduction and evolution reactions. *Scientific reports* **2017,** *7* (1), 5266.
66. Y. Lu, Y. Wang, H. Li, Y. Lin, Z. Jiang, Z. Xie, Q. Kuang and L. Zheng, MOF-Derived Porous Co/C Nanocomposites with Excellent Electromagnetic Wave Absorption Properties. *ACS applied materials & interfaces* **2015,** *7* (24), 13604-13611.
67. P. Kuisma‐Kursula, Accuracy, precision and detection limits of SEM–WDS, SEM–EDS and PIXE in the multi‐elemental analysis of medieval glass. *X‐Ray Spectrometry: An International Journal* **2000,** *29* (1), 111-118.
68. Z. Xie and Y. Wang, Metal-organic framework-derived CoNi-embedded carbon nanocages as efficient electrocatalysts for oxygen evolution reaction. *Ionics* **2017,** *24* (6), 1773-1780.
69. L. Shen, Q. Che, H. Li and X. Zhang, Mesoporous NiCo2O4Nanowire Arrays Grown on Carbon Textiles as Binder-Free Flexible Electrodes for Energy Storage. *Advanced Functional Materials* **2014,** *24* (18), 2630-2637.
70. C. Luo, J. Li, S. Tong, S. He, J. Li, X. Yang, X. Li, Y. Meng and M. Wu, Facile and scalable carbon-and binder-free electrode materials for ultra-stable and highly improved Li–O 2 batteries. *Chemical communications* **2018,** *54* (23), 2858-2861.
71. D.-H. Ha, M. A. Islam and R. D. Robinson, Binder-free and carbon-free nanoparticle batteries: a method for nanoparticle electrodes without polymeric binders or carbon black. *Nano letters* **2012,** *12* (10), 5122-5130.
72. G.-F. Chen, T. Y. Ma, Z.-Q. Liu, N. Li, Y.-Z. Su, K. Davey and S.-Z. Qiao, Efficient and Stable Bifunctional Electrocatalysts Ni/Ni

x

M

y

(M = P, S) for Overall Water Splitting. *Advanced Functional Materials* **2016,** *26* (19), 3314-3323.

73. M. Prabu, K. Ketpang and S. Shanmugam, Hierarchical nanostructured NiCo2O4 as an efficient bifunctional non-precious metal catalyst for rechargeable zinc-air batteries. *Nanoscale* **2014,** *6* (6), 3173-3181.
74. M. Tahir, L. Pan, R. Zhang, Y.-C. Wang, G. Shen, I. Aslam, M. A. Qadeer, N. Mahmood, W. Xu, L. Wang, X. Zhang and J.-J. Zou, High-Valence-State NiO/Co3O4 Nanoparticles on Nitrogen-Doped Carbon for Oxygen Evolution at Low Overpotential. *ACS Energy Letters* **2017,** *2* (9), 2177-2182.
75. H.-Y. Wang, Y.-Y. Hsu, R. Chen, T.-S. Chan, H. M. Chen and B. Liu, Ni3+-Induced Formation of Active NiOOH on the Spinel Ni-Co Oxide Surface for Efficient Oxygen Evolution Reaction. *Advanced Energy Materials* **2015,** *5* (10), 1500091.
76. J. Wang, J. Liu, D. Chao, J. Yan, J. Lin and Z. X. Shen, Self-assembly of honeycomb-like MoS2 nanoarchitectures anchored into graphene foam for enhanced lithium-ion storage. *Advanced materials* **2014,** *26* (42), 7162-7169.
77. Q. Wang, B. Zhao, S. Zhang, X. Gao and C. Deng, Superior sodium intercalation of honeycomb-structured hierarchical porous Na3V2(PO4)3/C microballs prepared by a facile one-pot synthesis. *Journal of Materials Chemistry A* **2015,** *3* (15), 7732-7740.
78. X. Wu, L. Jiang, C. Long and Z. Fan, From flour to honeycomb-like carbon foam: Carbon makes room for high energy density supercapacitors. *Nano Energy* **2015,** *13*, 527-536.